

<https://doi.org/10.1038/s43247-024-01267-0>

Magma budget, plutonic growth and lateral spreading at Mt. Etna

Mimmo Palano ^{1,2,3} ✉, Giuseppe Pezzo ⁴ & Claudio Chiarabba ⁴

The quantitative estimation of eruptible magma is essential to assess volcanic hazard. In case of high and frequent volcanic activity, different episodes and cycles can be observed and used to gain insights on magma residence and volcano dynamics. Here, by using surface ground deformation for 26 inflation and 14 deflation phases at Mt. Etna, we inferred two partially overlapping magmatic reservoirs located beneath the summit area in the 4–9 km (inflation sources) and in the 3–6 km (deflating sources) depth ranges. Our geodetic models highlight a continuous magma supply of $10.7 \times 10^6 \text{ m}^3/\text{yr}$ that took place in the last two decades. About 28.5% of this magma (i.e. volume loss inferred by geodetic models) contributed to the effusive activity at the surface, while the remaining 71.5% fed the endogenous volumetric growth of the plutonic crystallized mush and promoted the lateral spreading of Mt. Etna. The consistency of this behavior through time sets strong constraints on the eruptible quantity of magma in forecasting activity during a paroxysm.

The eruptive cycle paradigm (inflation–eruption–deflation¹) assumes that the influx of new magma and/or volatile exsolution leads to the pressurization of a magmatic reservoir and the inflation of the volcanic edifice. When the internal pressure exceeds the strength of the reservoir wall, the wall breaks, and magma ascends through conduits or dikes toward the surface, feeding the eruption. The subsequent drainage of magma and volatiles from the reservoir releases overpressure, causes edifice deflation, and terminates the eruption. After a repose period of weeks to years, the cycle begins anew. In such a context, long time-series of ground deformation data can capture one or more eruptive cycles, by tracking subsurface fluid (i.e. magma, volatiles, or hydrothermal waters) movements within the crust and allowing quantitative constraints on the geometry, size, and depth range of magmatic reservoirs. Valuable examples come from Soufriere Hills², Aktun^{3,4}, Westdahl⁴, Makushin⁴, Axial Seamounts⁵, Sierra Negra and Fernandina^{6–9}, Piton de la Fournaise¹⁰. These extensive datasets also help in defining the spatial and temporal patterns of flank instability, a major hazard affecting active volcanoes such as Kilauea (Hawaii, USA), Piton de la Fournaise (Reunion Island), Cumbre Vie (La Palma, Canary Islands), Mt. Etna (Italy), with the triggering of large landslides, tsunamis, and earthquakes¹¹.

A step forward is to track magma stagnation and migration during eruptive cycles by coupling deformation data with tomographic images of the plumbing system. The location and estimation of stored magma volumes provide constraints on deep recharging processes and on the

estimation of the magma budget entering/leaving the system. Obtaining consistent budget estimates is crucial to understanding if the replenishment of fresh magma within the stagnation levels occurs continuously or with episodic batches. One of the most desirable aspects is to estimate the volume of magma residing at shallow depths that could be mobilized by episodic supplies or sharp deformation at the volcano.

The exceptionally high volcanic activity continuously monitored by GNSS observations and the detailed definition of the plumbing system by tomography make Mt. Etna a paradigmatic example to compute such volumetric estimates. Mt. Etna is one of the most monitored volcanoes in the world with an almost continuous eruptive activity extending from its summit craters and fairly frequent lava flow eruptions to fissures opened up on its flanks (Fig. 1). The volcano built up since 500 ka¹² on the Apennine–Maghrebian accretionary wedge (Fig. 1a) near the Malta escarpment, a fault system separating the thinner Ionian oceanic lithosphere from the thicker continental crust of the Hyblean foreland, at the convergent margin between the Eurasia and Africa plates¹³. The origin of Mt. Etna is explained either as a passive asthenospheric mantle upwelling through a lithospheric tearing occurring at the south-western edge of the Calabrian subduction system^{13,14} or as a laterally feeding from a melt pooling region located below the Malta Escarpment fault system¹⁵. The volcano has a central conduit, with five summit craters located westward of the Valle del Bove depression (Fig. 1b). Three rift zones radiate from the summit following the locations and orientations of pyroclastic cones and eruptive fissures (Fig. 1c). Two of them,

¹Istituto Nazionale di Geofisica e Vulcanologia, Osservatorio Etneo, Catania, Italy. ²Dipartimento di Scienze della Terra e del Mare, Università degli Studi di Palermo, Palermo, Italy. ³Consiglio Nazionale delle Ricerche, IGAG, Roma, Italy. ⁴Istituto Nazionale di Geofisica e Vulcanologia, Osservatorio Nazionale Terremoti, Roma, Italy. ✉e-mail: mimmo.palano@unipa.it

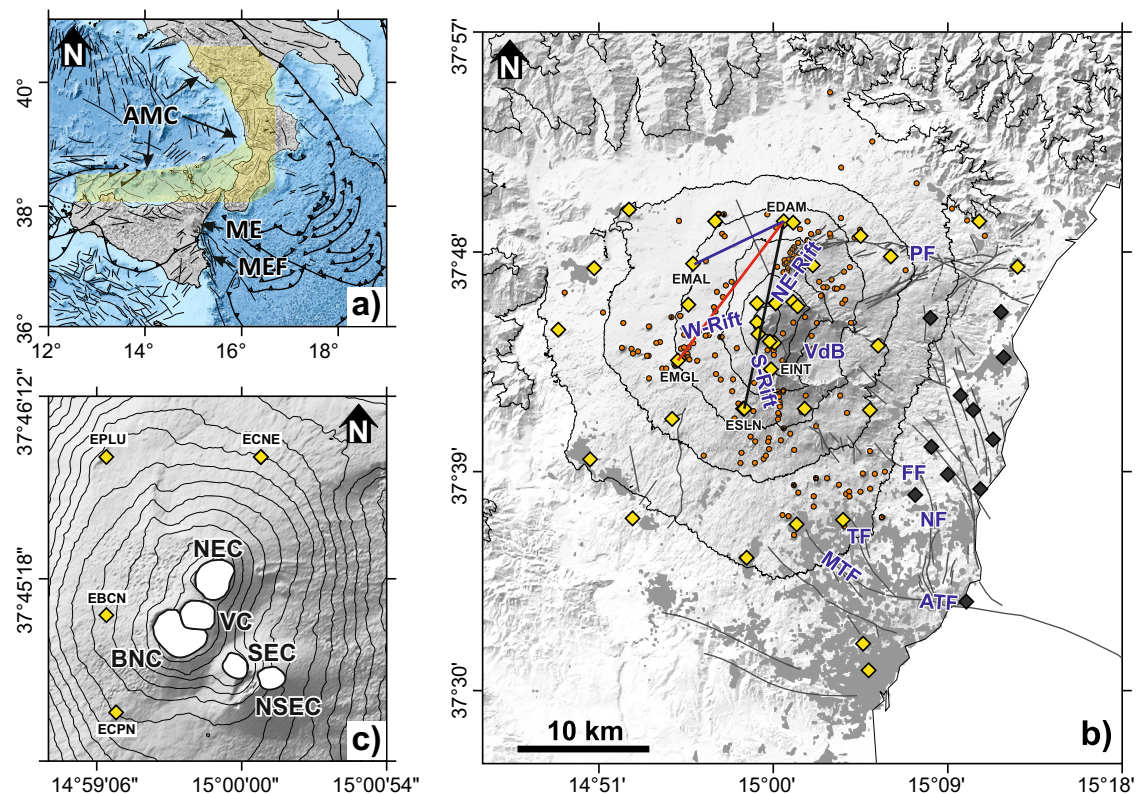


Fig. 1 | Location of the study area. **a** Map of southern Italy. ME Mt. Etna, AMC Apennine-Maghrebian chain, MEF Malta Escarpment fault system. **b** Sketch map of Mt. Etna volcano showing the urbanized areas (gray polygons) and main faults and tectonic lineaments (dark gray lines). The continuous GNSS network is also reported: yellow diamonds, stations used to constrain the elastic models discussed in this study; dark gray diamonds, remaining stations. The orange dots represent

pyroclastic cones, while active faults and tectonic lineaments are reported as gray lines. EDAM–ESLN, EDAM–EMAL, and EDAM–EMGL are reported as black, red, and blue lines, respectively. **c** Zoom of the summit area of Mt. Etna⁹¹. NEC North-East Crater, VC Voragine Crater, BNC Bocca Nuova Crater, SEC South-East Crater, NSEC New South-East Crater.

e.g. the North-East and the South rift zones, defining an overall NE-SE arcuate shape passing through the summit area, have guided the magmatic intrusions and the lateral eruptions in the last 20 years. This arcuate summit rift connects with faults edging a 25 km-wide horseshoe-shaped region (Fig. 1c), i.e. the unstable flank of the volcano¹⁶. The seaward motion of this sector of the volcano has been documented since the early 1980s¹⁷ and is temporally modulated by vigorous volcanic activity¹⁸.

Results

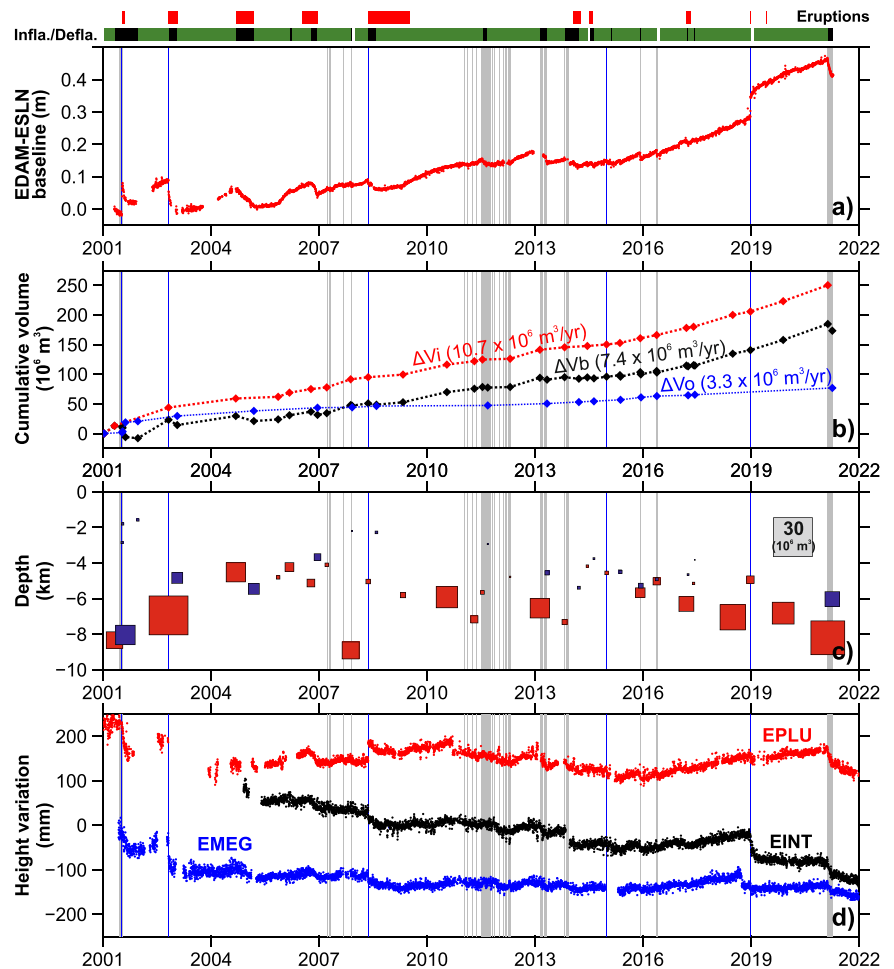
On an active volcano, the GNSS stations close to the crater area are sensitive to magma movement along the plumbing system, and therefore they represent an efficient way to detect changes in the behavior of the volcano¹. This is usually performed by inspecting the motion of one or more stations over time. To this end, we considered the change in distance (or baseline) between some continuous GNSS stations closely located in the summit area to investigate the January 2001–April 2021 period. We selected the EDAM and ESLN long-lived stations, which are located northward and southward of the summit area, respectively (Fig. 1). The EDAM–ESLN baseline time-series records a general lengthening (i.e. a growth of slope distance between the two stations) at a rate of ~ 20.7 mm/yr. Moreover, it distinctly shows non-linear motion with increasing and/or decreasing rates, well-evidencing the vivid activity of the volcano during the whole considered time interval (Fig. 2a). By inspecting the time-series, we detected several moderate-to-dramatic changes in rates with no uniform duration, mostly corresponding to marked variations in the volcanic activity. By coupling these observations with volcanological observations and other GNSS baselines (e.g. EDAM–EMGL and EDAM–EMAL; see the “Methods” section and Supplementary information), we defined a total of 57 different ground deformation phases, consisting of 28 inflation phases, 21 deflation phases, 5

magmatic intrusions and 3 periods with no significant deformation. Roughly speaking, each intrusion/eruptive phase was preceded by a recharge phase characterized by one or more inflation phases (in case of changes in the inflation rate) and then accompanied by a deflation phase during the lava discharge. The inflation phases are characterized by an average duration of ~ 220 days and cover up to 83.2% (16.85 years) of the entire investigated period. As previously mentioned, some inflations have been defined by a change in the inflation rate within a longer recharge phase (T12–T13, T17–T18, T24–T25–T26–T27, T29–T30, T52–T53, and T55–T56). Since January 2001, the longest recharge phase spans the August 2008–July 2011 (~ 2.94 years) and the late December 2018–February 2021 (~ 2.14 years) time intervals. The deflation phases are characterized by an average duration of ~ 54 days and span up to 18.4% (3.1 years) of the analyzed period. By considering the overall recharge/discharging phases, we defined 19 eruptive cycles (Supplementary Table 1).

Some of the inflation and deflation phases are characterized by weak signals and data fail in constraining elastic models (see Supplementary Table 1). By excluding these phases as well as those characterized by magmatic intrusions (generally related to fast migration of magma toward the surface in the last 2–3 km) and/or null deformation, we computed elastic deformation models for 26 inflation and 14 deflation phases (see the “Methods” section). Achieved results for each modeled phase (Figs. 2, 3 and Supplementary Table 1), allow an accurate investigation of the volcano’s behavior over the last 20 years.

All the sources are located beneath the summit area in the 3–9 km depth interval, with a clear spatial separation between inflation (depth range 4–9) and deflation (depth range 3–6) sources (Fig. 3). Such a different location suggests a connection between two different magmatic reservoirs, along which magma uprising is facilitated during each eruptive cycle.

Fig. 2 | Data and results. Time-series of volcanic activity (at the top: eruptive periods as red boxes, inflation and deflation phases as green and black boxes, respectively; inside the panels: shallow intrusions and lava fountaining episodes as blue and gray vertical lines, respectively) and geophysical data and results. **a** EDAM–ESLN baseline (see Fig. 1 for stations location). **b** Time-series of estimated ΔV_i , ΔV_o , and ΔV_b . Estimated average rates are also reported. **c** Depth variations of the inflation (red) and deflation (blue) modeled sources. These last are sized according to the estimated volume. **d** Height variations of EPLU (red), EINT (black), and EMEG (blue) stations.



Another implication is that the volcano has a replenishment phase preceding all eruptions (Fig. 2a). Estimated volume ranges between 1 and $30.8 \times 10^6 \text{ m}^3$ for the inflation phases and between 0.7 and $15.4 \times 10^6 \text{ m}^3$ for the deflation ones (Supplementary Table 1), highlight a vivid magma movement along the multilevel plumbing system of Mt. Etna. All the modeled sources have a prolate spheroid shape with the average ratio between the minor and major axes of 0.43 and 0.26 , for deflation and inflation sources, respectively. These spheroids typically exhibit a predominant vertical elongation (dip $> 68^\circ$; Supplementary Table 1) and have major axes with a prevalent NE–SW orientation.

Discussion

Plumbing system and magmatic reservoirs

A magmatic system generally consists of one or more regions containing various amounts of melt^{19,20}. These regions develop throughout the crust and can be separated by sub-solidus rocks or be continuous and connected, vertically defining a multi-layered system. Over the last decades, petrological and geophysical data have provided detailed images of the Mt. Etna plumbing system as a gigantic and complex multi-level reservoir extending down to a depth of ca. 30 km . The deeper part has been inferred through petrological data with two main magmatic environments located, respectively, at 19 – 23 km and below 25 km depth^{21,22}. These two main magmatic environments coincide with a region of low P-wave velocity anomalies²³. The shallow (0 – 9 km) and intermediate depth (10 – 19 km) portions are dominated by a huge plexus of P-wave high-velocity body located in the central-southern sector of the volcano and extending from 18 km depth to the surface^{24–27}. In the shallower part, all geodetically detected pressure sources are located along the western border of the high-velocity body,

defining at least three different levels of magmatic stagnation and storage, at 0 – 2 ^{28–31}, 4 – 6 ^{28,32–36}, 7 – 9 km ^{37–39}, respectively. Most of these levels match well with the ones inferred by petrological studies^{21,22,40–42}. In the intermediate part, available petrological data inferred some magmatic environments located in the 10 – 12 ^{40,43–45} and 13 – 16 km depth interval^{21,22,42,46,47}. This last magmatic environment roughly coincides with the magmatic sources related to the long-term uplift of the volcano edifice⁴⁸. The magmatic reservoirs defining the shallower part of the magmatic system have been identified several times in the last 3 decades, while the ones defining the intermediate and deeper portions have been detected/inferred only occasionally.

We define here with unprecedented detail the spatial distribution of deformation sources for the past two decades of activity (Fig. 3a). We observe a clear spatial separation between the inflation and the deflation sources. In particular, the inflating sources are located beneath the north-western sector of the summit area in the 4 – 9 km depth range, while the deflating sources are located beneath the south-eastern sector of the summit area in the 3 – 6 km depth range (Fig. 3b). All these sources are located along the north-western edge of the crustal volume defined by the earthquake distribution at shallow depth (0 – 6 km) beneath the southern and eastern flanks of the volcano (Fig. 3b). Such a crustal volume mainly corresponds to the high-velocity body detected by the P-wave tomographies (Fig. 3c, d) published in the last two decades^{24–27}. Therefore, our modeled sources define a northwestern dipping and elongated body where fresh magma likely arises directly from the mantle and interacts with residing magma at shallow depth (Fig. 3b). The sources of deformation match well with the volume at the northern edge of the high-velocity crystallized plexus where transient low-velocities indicated the residence of magma during the most recent large

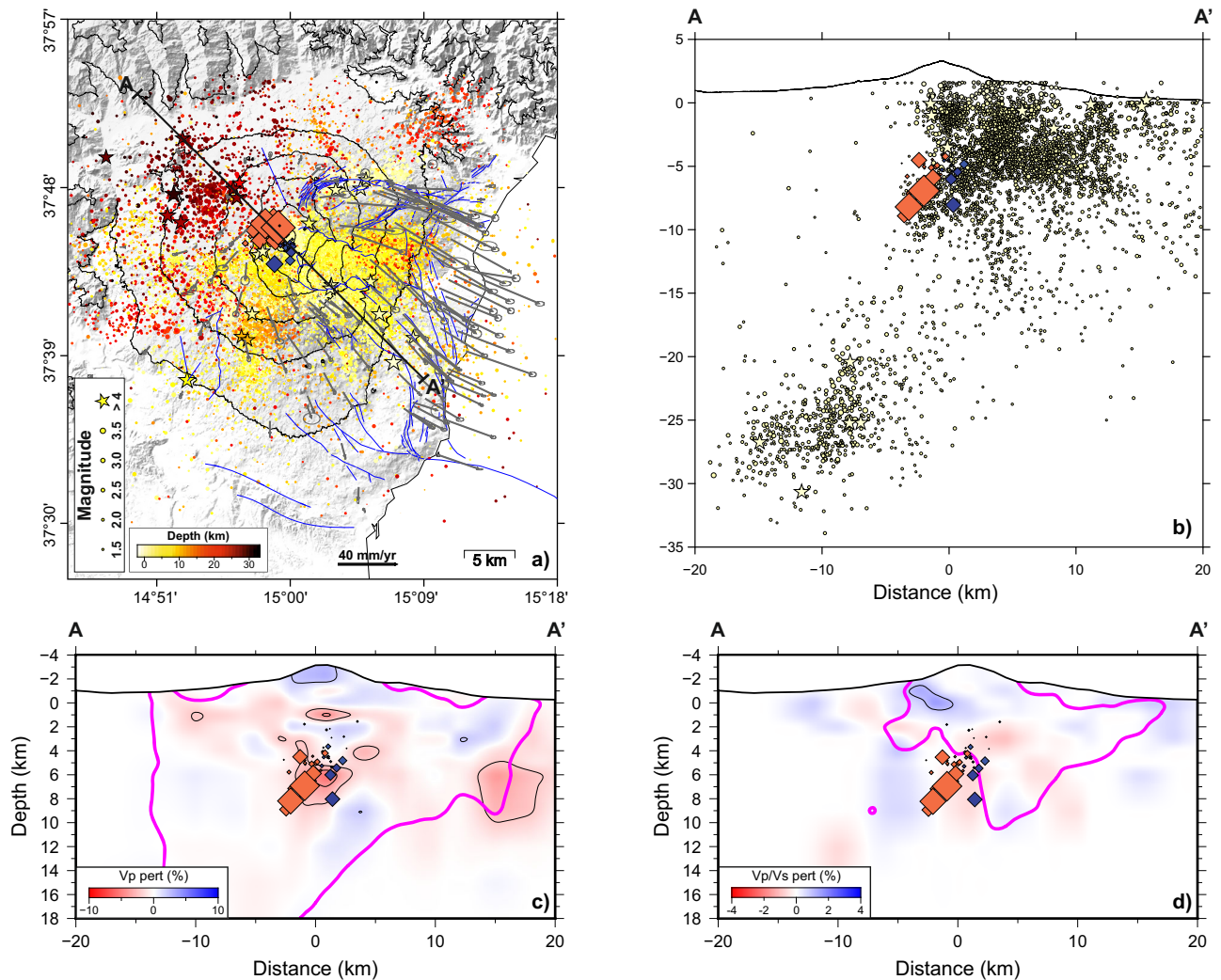


Fig. 3 | Comparison of geodetic results and seismological observations. **a** Seismicity ($M > 1$) occurring in the January 2000–April 2021 period (events with $M > 3.5$ are reported as stars); the modeled sources (sized according to the estimated volume and colored in red and blue for inflation and deflation phases, respectively; Supplementary Table 1) are also reported. The gray arrows represent the long-term (2004.42–2018.95) GNSS horizontal velocity field with 95% confidence ellipses⁸⁴. **b** Vertical A–A’ section showing the distribution in depth of seismicity and modeled

sources. **c** Vertical A–A’ section through the DVp time-lapse model²⁷. **d** Vertical A–A’ section through the DVp/Vs time-lapse model. The purple lines (panels c and d) represent the limit of the resolved volume. Note that the volume of transient low Vp corresponds to the deformation modeled sources defining the magma involved during inflations and deflations. The sources correspond to an area of loss of resolution of the Vp/Vs model because S-waves are strongly attenuated during their travel within the magma-filled volume.

eruptive episodes²⁷. Moreover, the northwestern dipping body closely resembles the active reverse structure beneath Mt. Etna⁴⁹, therefore suggesting that arising magma is controlled/channeled by inverse faults of the Apennine-Maghrebian accretionary wedge. Some studies have recently proven that magma arising toward the surface is a feasible mechanism also in coeval compressional settings^{50–52}. Valuable examples come from Guagua Pichincha, Ecuador⁵³, Socompa, Chile⁵⁴, and Taapaca, Chile⁵⁵.

The spatial separation between the inflation and the deflation sources is more evident at shallow depth, with the latter located beneath the south-eastern sector of the summit area. The continuous south-eastward motion of the unstable flank presumably led to a decrease in the confining pressure and an increase in host-rock porosity beneath the summit area and along the South and North-East rift zones. This mechanism would enable the formation of new pathways/reservoirs in the very shallow crust, also providing a plausible explanation for the south-eastward migration of the shallow deflation sources.

Volume estimation and magma compressibility

Geodetically estimated volumes are commonly considered as the injected volume of a magmatic fluid within the reservoir⁵⁶. For simplicity, we refer to

the positive (inflation) and negative (deflation) volume changes as magma input (ΔV_i) and magma output (ΔV_o), respectively. The former represents the deeply sourced magma entering into the plumbing system of the volcano, while the latter is the magma leaving the magmatic reservoir because of eruptive onsets at the surface. In the following, our estimated volumes must be considered as minimum estimates since we consider an isotropic elastic half-space medium with a Poisson’s ratio of 0.25.

A large quantity of magma (Fig. 2b, c) entered into the system during the inflation phases preceding the 2002–2003 lateral eruption (ca. $30.8 \times 10^6 \text{ m}^3$, T07 in Supplementary Table 1) and the lava fountains occurring during the 16 February–1 April 2021 period (ca. $27.0 \times 10^6 \text{ m}^3$, T56 in Supplementary Table 1). For these phases, the modeled sources are located in the 7–8.5 km depth range, at the bottom of the previously defined shallow part (0–9 km) of the plumbing system (Fig. 2c). Both phases follow two eruptive episodes, namely as the July–August 2001 lateral eruption (T06 in Supplementary Table 1) and the late December 2018 one (T54 in Supplementary Table 1) which generated large deformations along the South rift zone and the summit area, leading also to a large scale seaward motion of the eastern flank of the volcano^{32,57}. In this context, the drastic drop in pressure along the upper portion of the plumbing system created a pressure

imbalance with the deeper portions, favoring the ascent of fresh magma from depth during the post-eruptive inflations (T07 and T56). The ΔV_i time-series (Fig. 2b) also reveals that during the September 2004–February 2013 period, moderate quantities of magma (ca. $13\text{--}18 \times 10^6 \text{ m}^3$ for each inflation stage) entered in the system every 2.8 ± 0.3 years (e.g. T10, T18, T25, and T30; Supplementary Table 1), suggesting a quasi-cyclic recharge of the lower portion of the shallow plumbing system. Moreover, after a period characterized by inflations with small volume variations (April 2013–April 2015; e.g. T32, T34, T37, and T41), a magma accumulation resumed from May 2015 at increasing rates (T43, T45, T48, T52, T53, T55, and T56; Supplementary Table 1) highlighting impressive pressurization of the shallow plumbing system. Overall, the ΔV_i cumulative time-series defines a near-continuous magma accumulation in the feeding system at a rate of $10.7 \pm 0.3 \times 10^6 \text{ m}^3/\text{yr}$ (Fig. 2b).

By considering the ΔV_o time-series (Fig. 2b), the largest negative variation (ca. $15.4 \times 10^6 \text{ m}^3$; T05 on Supplementary Table 1) occurred during the July–August 2001 eruption, while moderate variations were observed during the 2002–2003 lateral eruption (ca. $8.7 \times 10^6 \text{ m}^3$; T09 on Supplementary Table 1), the 2004–2005 eruption (ca. $8.7 \times 10^6 \text{ m}^3$; T11 on Supplementary Table 1), and during the early 2021 lava fountains sequence (ca. $11.6 \times 10^6 \text{ m}^3$; T57 on Supplementary Table 1). The other deflation phases have been characterized by negative variations generally smaller than $5.0 \times 10^6 \text{ m}^3$ (Supplementary Table 1). Overall, the ΔV_o cumulative time-series defines a magma discharge occurring at a rate of $3.3 \pm 0.3 \times 10^6 \text{ m}^3/\text{yr}$ (Fig. 2b), evidencing how during the investigated time interval only 28.5% of the magma entered into the magmatic system (ΔV_i) was drainage during the deflation phases. Therefore, this percentage could be considered a realistic measure of the possible eruptible quantity of magma during each eruptive cycle. By combining the ΔV_i and ΔV_o quantities over time, we can estimate the balance (ΔV_b) between the magma entering and leaving the storage system. Such a balance is not constant over time (Fig. 2b) but showed phases of major magma accumulation and drainage. As previously observed, the balance is positive and defines a net magma supply of $7.4 \pm 0.3 \times 10^6 \text{ m}^3/\text{yr}$ (Fig. 2b) resulting in a continuous accumulation of magma along the plumbing system of the volcano, and in turn in the volumetric growth of the volcano edifice. This vigorous and continuous magma accumulation concurs well with the marked eruption frequency increase observed at least since 1975⁵⁸.

Erupted magma is one of the main volcanic outputs and its volume has been compared with the volume change measured by geodetic measurements on several active volcanoes^{59–63}. Observed eruptive volumes are commonly 1–8 times larger than the geodetically modeled ones during volcanic eruptions^{61–66}. This is also the case for Mt. Etna, where our estimated magma discharge (ca. $3.3 \pm 0.3 \times 10^6 \text{ m}^3/\text{yr}$) is lower than the one estimated by field measurements and satellite observations^{67–71}. In particular, the average magma output rate of $25 \times 10^6 \text{ m}^3/\text{yr}$ estimated at Mt. Etna for the last 40 years⁶⁹ is 7.5 times larger than our estimated magma discharge.

Such a general discrepancy is related to new magma influx from the depth during eruptions and/or compressibility of magma. The influx of new magma from deep sources to shallow reservoirs could partially (or totally) balance the magma lost by the shallow reservoir during eruptive events. Alternatively, the deep magma could ascent along the plumbing system to be directly erupted at the surface. Both mechanisms provide a realistic explanation of the observed discrepancy and have been occasionally documented at Mt. Etna^{32,35}. Magma compressibility is also considered a main factor to explain the discrepancies between geodetic and erupted volumes. The compressibility of magma is largely controlled by the high pressures in the Earth's crust and the presence of highly compressible exsolving volatile phase⁷². Moreover, additional complexities come from the mechanical properties of the host rock which in turn depend on the presence of fractures and void spaces⁵⁶. The absence of comprehensive data regarding the compressibility and other critical physical parameters that characterize the bulk magma at Mt. Etna (e.g. density, magma composition, volatile contents in the melt, gas volume fraction, etc.) has hindered establishing

well-defined relationships. However, CO_2 is thought to become exsolved at considerable depth⁷³, suggesting the presence of a significant amount of volatiles in the magmatic reservoirs at Mt. Etna. Indeed, CO_2 emission at Mt. Etna contributes to 10% of the global volcanic emission and greatly exceeds the amount that can be dissolved in the erupted magma⁷⁴, suggesting external contributions such as mantle-derived fluids and/or assimilation of Mesozoic carbonates⁷⁵. The development of ground- and satellite-based techniques has notably improved the measurements of SO_2 flux over several active volcanoes, increasing the availability of long-time series and catalogs⁷⁶. By comparing volume estimations derived from thermal and SO_2 flux satellite measurements with the geodetically derived ones for the 2004–2007 period, Coppola et al.⁷⁷ found an excellent correlation and inferred a ratio between the two estimates ranging from 2.4 to 6.5, with a best-fit value of 3.6. This agreement is considerably promising and suggests that more accurate estimations on magma budget may be readily achieved in the future by considering geodetic and geochemical data, along with other observables as ground SO_2 flux measurements. However, it also highlights that magma compressibility varies greatly over time, especially during an eruption. Therefore, long-time series of data are needed to achieve accurate estimations. Furthermore, Calvari et al.⁷⁸, by comparing the volume of erupted magma at Mt. Etna from 2016 to 2020 with respect to the expected one from its average eruptive rate, suggested the accumulation of magma beneath the volcano. This aspect matches well with our results which evidenced an impressive pressurization of the shallow plumbing system of the volcano since May 2015 (Supplementary Table 1).

All these features highlight that rapid and accurate estimations of magma budget on active volcanoes like Mt. Etna are of considerable interest and impact on territory management since they can provide useful constraints on possible eruptive events in terms of eruptible magma and volcanic risk assessment.

Height variations and lateral spreading

The elastic models predict a general vertical growth of the volcanic edifice, continuous during almost the entire investigated period. The vertical growth is vigorous, despite episodically being interrupted by local-to-volcano-scale subsidence related to the short-term deflation phases. However, the time-series of vertical components of stations located around the summit area (EPLU and EINT; red and blue time-series in Fig. 2d, respectively) and on the upper western flank of the volcano (EMEG; black time-series in Fig. 2d), show long-term subsidence, despite cyclic (EPLU station) or episodic (EMEG and EINT stations) transients. EPLU and EMEG show a subsidence of $\sim 5 \text{ mm}/\text{yr}$ and most of the observed vertical motion occurred before the 2002–2003 eruption, while EINT exhibits a near continuous subsidence of $\sim 11 \text{ mm}/\text{yr}$. EPLU and EINT stations are externally located with respect to the small N-S elongated graben-like structure inferred by Murray et al.⁷⁹, therefore their behavior is not (or little) influenced by the strong subsidence measured within the graben ($\sim 4 \text{ m}$ during the August 1975–September 2018 period). Moreover, the overall subsiding pattern along with the near continuous magma accumulation beneath the volcano suggests that the volumetric growth of the edifice is dominantly horizontal. The long-term picture of Mt. Etna deformation shows an inhomogeneous pattern with the largest rates measured on the eastern flank of the volcano (Fig. 3a). An increase in the horizontal motion moving away from the volcano summit can be recognized, suggesting a gravitational control on the southeastward spreading of the edifice^{18,57}. Such an asymmetric spreading pattern is controlled by the basement topography beneath the volcano and the SE gently dipping shallow interface between rocks and Quaternary sediments¹². Moreover, the buttressing of the volcano by the Apennine-Maghrebian chain prevents the spreading toward the north and west. In such a context, the steady-state seaward motion of the eastern flank induces a progressive depressurization of the crust beneath the rift areas, encouraging the deep resourcing of magma and its accumulation in the shallower part of the plumbing volcano, contributing therefore to the endogenous growth of the plutonic complex (the high P-wave velocity body) beneath Mt. Etna volcano.

Conclusions

We demonstrate here that volumetric estimates of the magma budget entering and leaving a volcanic system are now possible and provide constraints in forecasting volcanic activity during sharp episodes or activity climaxes. We tracked magma movements within Mt. Etna's plumbing system, revealing a continuous magma supply from a depth of ca. $10.7 \times 10^6 \text{ m}^3/\text{yr}$ over a period of almost two decades. The enveloped geometry of the deformation sources suggests that the final rising of magma through the crust is controlled by an NW-dipping interface that we hypothesize is a structure of the compressional belt. About 28.5% of this magma contributed to the decennial effusive activity, providing a valuable constraint on the eruptible quantity of magma during each eruptive cycle. The remaining quantity (ca. 71.5%) is stored within the plumbing system and contributes to the endogenous volumetric growth of the plutonic crystallized mush, and in turn, to the lateral spreading of Mt. Etna.

The huge amount of stocked magma beneath stratovolcanoes raises new questions on whether they could be remobilized to feed eruptions by episodes of sharp deformation or unrest. Increasingly tight constraints on the volume of magma will also substantially improve our understanding of the magmatic systems, revolutionizing the volcanic hazard assessment. At Mt. Etna, the huge quantity of magma would lead to a substantial increase of volcanic activity both from the summit area as well as from the volcano flanks. The occurrence of lateral eruptions dramatically increases the hazard, especially for the potential opening of eruptive fractures on the lower slopes of the volcano^{80,81}, where almost a million people live. Moreover, the continuous magma accumulation increases the probability of a seaward acceleration of the unstable flank of the volcano, and the occurrence of moderate earthquakes at very shallow depths, as already observed during the 2002–2003 and 2018 eruptive events^{57,82}. On a kyr scale, the prolonged accumulation of magma in the shallow crust would potentially lead to catastrophic flank instability episodes, triggering in turn tsunamis that can hit the densely populated coasts surrounding the eastern Mediterranean Sea. A similar episode occurred in the early Holocene, probably related to the collapse of the Valle del Bove⁸³.

Achieved results can be easily exported and compared with the ones coming from other densely monitored volcanoes, as well as used to validate/integrate the available information on most of the other worldwide active volcanoes where the monitoring system is spatially and temporally limited.

Methods

GNSS network and data processing

The setting up of a continuous GNSS network at Etna began in November 2000, reaching a configuration of 13 stations in the late summer of 2001 with a daily session of ~8 h. The network geometry was gradually upgraded over the years in order to cover all the slopes of the volcano edifice and to replace the sites destroyed by natural (lava flows) and human (vandalism) activities or affected by local instability, reaching the current configuration of 33 stations (Fig. 1). The upgrade was also coupled with a general improvement of technologies (e.g. receivers, antennas, real-time data streaming and long-term power supply—typically a combination of batteries and solar panels at remote sites), therefore allowing continuous acquisition on sessions of 24 h, at least since early 2005. Raw GNSS observations, collected since November 2000, were processed by using the GAMIT/GLOBK software (<http://geoweb.mit.edu/gg/>) and by adopting the same strategy described in Palano et al.⁸⁴. Achieved results as daily coordinates (i.e. time-series) and velocity fields have been referred to the MERF23 frame⁸⁴. This reference frame allows to isolate the Mt. Etna volcanic deformation from the background tectonic pattern and enable a direct combination and comparison between different deformation phases (inflation, deflation, dike intrusion) affecting the volcano edifice over time.

GNSS time-series analyses and data modeling

Among the available GNSS baseline, we considered the EDAM–ESLN one since it has very few data gaps over the April 2001–April 2021 period (Figs. 1 and 2). This baseline is very sensitive to magma movements along the

plumbing system allowing to capture with fine detail any change in the volcano behavior. The baseline is generally affected by lengthening during the inflation phases and shortening during the deflation ones. However, to properly define some deformative phases on periods not adequately covered by the EDAM–ESLN baseline (e.g. T01, T06, T07, T09, and T10), we also considered two additional baselines, namely the EDAM–EMGL and EDAM–EMAL ones (see supplementary material). By inspecting these time-series, we detected several moderate-to-drastic changes in rates with no uniform duration, mostly corresponding to marked variations in the volcanic activity (<https://www.ct.ingv.it/index.php/monitoraggio-e-sorveglianza/prodotti-del-monitoraggio/bollettini-settimanali-multidisciplinari>). On the basis of geodetic data and volcanological observations (Supplementary Table 2), we defined a total of 57 different ground deformation phases consisting of 28 inflation phases, 21 deflation phases, 5 magmatic intrusions and 3 periods with no significant deformation (Supplementary Table 1). Most of these phases show piecewise linear segments on the analyzed baselines suggesting inflation or deflation with constant rates, while some are characterized by nonlinear segments, denoting complex deformation patterns. These phases include both inflations (T15, T18, T25, T48, T50, and T55) and deflations (T09, T16, T19, T23, T31, and T33), and are related to short-term volcanic activities (e.g. lava fountaining, passive lava effusion, strombolian activity, etc.). The geodetic signals related to these short-term volcanic activities are generally small (with a low signal/noise ratio) and are not pertinent to the general questions addressed in this study. Therefore, in the following, we considered the phases including these short-term volcanic activities as homogeneous in terms of ground deformation patterns. For each detected phase, we estimated the ground deformation field in terms of geodetic velocities by combining the daily GAMIT solutions into a consistent set of station positions and velocities, referred to MERF23⁸⁴.

Looking at the estimated surface geodetic velocities, some of the inflation and deflation phases are characterized by weak signals and perhaps poorly able to constrain elastic models (see Table S1 and figures in the Supplementary material). By excluding these phases as well as those characterized by magmatic intrusions (generally related to fast migration of magma toward the surface in the last 2–3 km) and/or null deformation, in the following, we computed elastic deformation models for 26 inflation and 14 deflation phases.

The surface deformation for each of these phases was used to constrain isotropic half-space elastic inversion models by adopting a uniform approach in order to define all modeled parameters in a robust and unambiguous way over the studied period and to allow a direct comparison between the obtained results. To this end, the inversions were performed by adopting the following uniform approach:

- to properly model the asymmetric surface ground deformation patterns, as commonly observed at Mt. Etna³², we adopted the analytical formulation related to a spheroidal pressure source⁸⁵. This source is determined by eight parameters: location (longitude, latitude, and depth) of the center of the spheroid, strike, and dip of the major semi-axis a , length of the major semi-axis a , ratio b/a between the minor (b) and major (a) axes, and the pressure change required to produce the observed surface deformation;
- values of 30 GPa and 0.25 were assumed for the shear modulus (μ) and Poisson's ratio in the half-space, respectively;
- since Mt. Etna volcano is characterized by significant topography, the effects of topography have been included in each computation⁸⁶;
- both horizontal and vertical GNSS components were inverted by taking into account the weights proportional to the estimated geodetic velocity errors;
- to obtain realistic estimations of the pressure change parameter, we limited the ratio of the pressure change to the shear modulus within the elastic limits of the surrounding rock;
- the model parameters optimization was performed by using a genetic algorithms methodology⁸⁷, an approach which starting with an initial range of models, progressively modifies the solution by incorporating

the evolutionary behavior such as the biological systems. The fitness of each solution is measured by a quantitative, objective function, i.e., a measure of the discrepancy (χ^2) between the measurements and the predicted values from the model, defined as: $\chi^2 = \sum_i^N \left[\frac{(O_i - P_i)}{e_i} \right]^2$, where O_i is measured value, P_i is the predicted value from the model, e_i is the uncertainty associated to each measured value and $i = 1, \dots, N$, the total number of measurements;

- all sites located on the lower portion of the unstable flank of the volcano (marked as dark gray polygons in Fig. 1b) have been excluded from the inversion because of their continuous seaward motion⁸⁴. Sites located on the middle-to-upper portion of the unstable flank have been included in the inversion: while they provide a better geometry to constrain the parameters of the modeled source, the expected deformation at their location is generally lower than the observed one, resulting in a poor fit of the model. By using these stations, a possible bias of the parameters of the modeled source would be introduced; however, by considering the general good fit at the stations located externally from the unstable flank of the volcano (Supplementary material), we believe that such a bias can certainly be considered negligible.

For each modeled phase, the volume change of the ellipsoidal cavity has been estimated by adopting the following empirical formulation: $\Delta V = \frac{3V\Delta P}{4\mu} \left(\frac{A^2}{3} - cA + d \right)$ where V is the volume of the ellipsoidal cavity, ΔP is the pressure change, $A = b/a$ represents the geometric aspect ratio between the semi-minor axis b and the semi-major axis a of analytical spheroidal pressure source⁸⁵. Constants c and d have been determined by the polynomial best fit to the numerical solutions spheroidal⁸⁸ and have values of 0.7 and 1.37, respectively. The estimated volume can be considered a minimum estimation since we considered a medium with a Poisson ratio of 0.25. The uncertainties of the best fitting parameters were estimated by adopting a Jackknife sampling method⁸⁹. Best fitting parameters for each modeled phase, along with the estimated uncertainties, are reported in Supplementary Table 1.

Data availability

Data, observations and reports related to the volcanic activity of Mt. Etna volcano are available at <https://www.ct.ingv.it/index.php/monitoraggio-e-sorveglianza/prodotti-del-monitoraggio/bollettini-settimanali-multidisciplinari>. The seismic data are available at <https://www.ct.ingv.it/index.php/monitoraggio-e-sorveglianza/banche-dati-terremoti/terremoti>. Other data are available at <https://doi.org/10.5281/zenodo.10557119>.

Received: 2 August 2023; Accepted: 12 February 2024;

Published online: 21 February 2024

References

- Dzurisin, D. A comprehensive approach to monitoring volcano deformation as a window on the eruption cycle. *Rev. Geophys.* **41**, 1001 (2003).
- Mattioli, G. S. et al. Long term surface deformation of Soufrière Hills Volcano, Montserrat from GPS geodesy: inferences from simple elastic inverse models. *Geophys. Res. Lett.* **37**, L00E13 (2010).
- DeGrandpre, K., Wang, T., Lu, Z. & Freymueller, J. T. Episodic inflation and complex surface deformation of Akutan volcano, Alaska revealed from GPS time-series. *J. Volcanol. Geotherm. Res.* **347**, 337–359 (2017).
- Xue, X. & Freymueller, J. T. A 25-year history of volcano magma supply in the east central Aleutian arc, Alaska. *Geophys. Res. Lett.* **47**, e2020GL088388 (2020).
- Nooner, S. L. & Chadwick, W. W. Jr Inflation-predictable behavior and co-eruption deformation at Axial Seamount. *Science* **354**, 1399–1403 (2016).
- Gregg, P. M. et al. Stress triggering of the 2005 eruption of Sierra Negra Volcano, Galápagos. *Geophys. Res. Lett.* **45**, 13–288 (2018).
- Gregg, P. M. et al. Forecasting mechanical failure and the 26 June 2018 eruption of Sierra Negra volcano, Galápagos, Ecuador. *Sci. Adv.* **8**, eabm4261 (2022).
- Bagnardi, M. & Amelung, F. Space-geodetic evidence for multiple magma reservoirs and subvolcanic lateral intrusions at Fernandina Volcano, Galápagos Islands. *J. Geophys. Res.* **117**, B10406 (2012).
- Galetto, F., Reale, D., Sansosti, E. & Acocella, V. Implications for shallow magma transfer during the 2017 and 2018 eruptions at Fernandina (Galápagos) inferred from InSAR data. *J. Geophys. Res. Solid Earth* **128**, e2022JB026174 (2023).
- Peltier, A. et al. Cyclic magma storages and transfers at Piton de La Fournaise volcano (La Réunion hotspot) inferred from deformation and geochemical data. *Earth Planet. Sci. Lett.* **270**, 180–188 (2008).
- McGuire, W. J. Volcano instability: a review of contemporary themes. *Geol. Soc. Lond. Spec. Publ.* **110**, 1–23 (1996).
- Branca, S. & Ferrara, V. The morphostructural setting of Mount Etna sedimentary basement (Italy): implications for the geometry and volume of the volcano and its flank instability. *Tectonophysics* **586**, 46–64 (2013).
- Gvirtzman, Z. & Nur, A. The formation of Mount Etna as the consequence of slab rollback. *Nature* **401**, 782–785 (1999).
- Dogliani, C., Innocenti, F. & Mariotti, G. Why Mt Etna? *Terra Nova* **13**, 25–31 (2001).
- Neri, M., Rivalta, E., Maccaferri, F., Acocella, V. & Cirrincione, R. Etnean and Hyblean volcanism shifted away from the Malta Escarpment by crustal stresses. *Earth Planet. Sci. Lett.* **486**, 15–22 (2018).
- Palano, M. et al. Slow slip events and flank instability at Mt. Etna volcano (Italy). *Tectonophysics* **836**, 229414 (2022).
- Borgia, A., Ferrari, L. & Pasquarè, G. Importance of gravitational spreading in the tectonic and volcanic evolution of Mount Etna. *Nature* **357**, 231–235 (1992).
- Pezzo, G. et al. Coupling flank collapse and magma dynamics on Stratovolcanoes: the Mt. Etna example from InSAR and GNSS observations. *Remote Sens.* **15**, 847 (2023).
- Sparks, R. S. J. et al. Formation and dynamics of magma reservoirs. *Philos. Trans. R. Soc. A* **377**, 20180019 (2019).
- Edmonds, M., Cashman, K. V., Holness, M. & Jackson, M. Architecture and dynamics of magma reservoirs. *Philos. Trans. R. Soc. A* **377**, 20180298 (2019).
- Giacomoni, P. P. et al. Mt. Etna plumbing system revealed by combined textural, compositional, and thermobarometric studies in clinopyroxenes. *Contrib. Mineral. Petrol.* **171**, 1–15 (2016).
- Cannata, A. et al. Space-time evolution of magma storage and transfer at Mt. Etna Volcano (Italy): the 2015–2016 reawakening of Voragine Crater. *Geochem. Geophys. Geosyst.* **19**, 471–495 (2018).
- Monna, S., Sgroi, T. & Dahm, T. New insights on volcanic and tectonic structures of the southern Tyrrhenian (Italy) from marine and land seismic data. *Geochem. Geophys. Geosyst.* **14**, 3703–3719 (2013).
- Chiarabba, C. et al. Recent seismicity and tomographic modeling of the Mount Etna plumbing system. *J. Geophys. Res. Solid Earth* **105**, 10923–10938 (2000).
- Laigle, M. et al. Mount Etna dense array local earthquake P and S tomography and implications for volcanic plumbing. *J. Geophys. Res. Solid Earth* **105**, 21633–21646 (2000).
- Patanè, D. et al. Time-resolved seismic tomography detects magma intrusions at Mount Etna. *Science* **313**, 821–823 (2006).
- Giampiccolo, E. Dyke intrusion and stress-induced collapse of volcano flanks: the example of the 2018 event at Mt. Etna (Sicily, Italy). *Sci. Rep.* **10**, 6373 (2020).
- Aloisi, M. et al. Imaging the multi-level magma reservoir at Mt. Etna volcano (Italy). *Geophys. Res. Lett.* **38**, L16306 (2011).

29. Patanè, D. et al. Insights into magma and fluid transfer at Mount Etna by a multiparametric approach: a model of the events leading to the 2011 eruptive cycle. *J. Geophys. Res. Solid Earth* **118**, 3519–3539 (2013).
30. Bonaccorso, A. et al. Eruptive processes leading to the most explosive lava fountain at Etna volcano: the 23 November 2013 episode. *Geophys. Res. Lett.* **41**, 4912–4919 (2014).
31. Greco, F. et al. Evidence of a shallow persistent magmatic reservoir from joint inversion of gravity and ground deformation data: the 25–26 October 2013 Etna lava fountaining event. *Geophys. Res. Lett.* **43**, 3246–3253 (2016).
32. Palano, M. et al. Magma transport and storage at Mt. Etna (Italy): a review of geodetic and petrological data for the 2002–03, 2004 and 2006 eruptions. *J. Volcanol. Geotherm. Res.* **347**, 149–164 (2017).
33. Bruno, V. et al. Ground deformations and volcanic processes as imaged by CGPS data at Mt. Etna (Italy) between 2003 and 2008. *J. Geophys. Res. Solid Earth* **117**, B07208 (2012).
34. Spampinato, L. et al. Multiparametric study of the February–April 2013 paroxysmal phase of Mt. Etna New South-East crater. *Geochem. Geophys. Geosyst.* **16**, 1932–1949 (2015).
35. Viccaro, M. et al. How a complex basaltic volcanic system works: constraints from integrating seismic, geodetic, and petrological data at Mount Etna volcano during the July–August 2014 eruption. *J. Geophys. Res. Solid Earth* **121**, 5659–5678 (2016).
36. Gambino, S. et al. The unusual 28 December 2014 dike-fed paroxysm at Mount Etna: timing and mechanism from a multidisciplinary perspective. *J. Geophys. Res. Solid Earth* **121**, 2037–2053 (2016).
37. Palano, M., Puglisi, G. & Gresta, S. Ground deformation patterns at Mt. Etna from 1993 to 2000 from joint use of InSAR and GPS techniques. *J. Volcanol. Geotherm. Res.* **169**, 99–120 (2008).
38. González, P. J. & Palano, M. Mt. Etna 2001 eruption: New insights into the magmatic feeding system and the mechanical response of the western flank from a detailed geodetic dataset. *J. Volcanol. Geotherm. Res.* **274**, 108–121 (2014).
39. Cannata, A. et al. Pressurization and depressurization phases inside the plumbing system of Mount Etna volcano: evidence from a multiparametric approach. *J. Geophys. Res. Solid Earth* **120**, 5965–5982 (2015).
40. Métrich, N. et al. 2001 flank eruption of the alkali-and volatile-rich primitive basalt responsible for Mount Etna's evolution in the last three decades. *Earth Planet. Sci. Lett.* **228**, 1–17 (2004).
41. Corsaro, R. A. & Pompilio, M. Buoyancy-controlled eruption of magmas at Mt Etna. *Terra Nova* **16**, 16–22 (2004).
42. Magee, R., Ubide, T. & Kahl, M. The lead-up to Mount Etna's most destructive historic eruption (1669). Cryptic recharge recorded in clinopyroxene. *J. Petrol.* **61**, egaa025 (2020).
43. Spilliaert, N., Allard, P., Métrich, N. & Sobolev, A. V. Melt inclusion record of the conditions of ascent, degassing, and extrusion of volatile-rich alkali basalt during the powerful 2002 flank eruption of Mount Etna (Italy). *J. Geophys. Res. Solid Earth* **111**, B0420 (2006).
44. Corsaro, R. A. et al. The 1974 flank eruption of Mount Etna: an archetype for deep dike-fed eruptions at basaltic volcanoes and a milestone in Etna's recent history. *J. Geophys. Res. Solid Earth* **114**, B07204 (2009).
45. Di Renzo, V. et al. Long and short-term magma differentiation at Mt. Etna as revealed by Sr-Nd isotopes and geochemical data. *Earth Sci. Rev.* **190**, 112–130 (2019).
46. Mollo, S. et al. Reconstruction of magmatic variables governing recent Etnean eruptions: constraints from mineral chemistry and P-T-fO₂-H₂O modeling. *Lithos* **212**, 311–320 (2015).
47. Ubide, T. & Kamber, B. S. Volcanic crystals as time capsules of eruption history. *Nat. Commun.* **9**, 326 (2018).
48. De Guidi, G. et al. New evidence for Late Quaternary deformation of the substratum of Mt. Etna volcano (Sicily, Italy): clues indicate active crustal doming. *Bull. Volcanol.* **76**, 1–13 (2014).
49. Barreca, G. et al. Slab detachment, mantle flow, and crustal collision in eastern Sicily (southern Italy): Implications on Mount Etna volcanism. *Tectonics* **39**, e2020TC006188 (2020).
50. Saint Blanquat, M., Tikoff, B., Teyssier, C. & Vigneresse, J. L. Transpressional kinematics and magmatic arcs. In *Continental Transpressional and Transensional Tectonics* (eds Holdsworth, R. E., Strachan, R. A. & Dewey, J. F.). *Geol. Soc. Lond. Special Publ.* **135**, 327–340 (1998).
51. Galland, O. et al. Magma-controlled tectonics in compressional settings; insights from geological examples and experimental modelling. *Boll. Soc. Geol. Ital.* **127**, 205–208 (2008).
52. Tibaldi, A. Contractual tectonics and magma paths in volcanoes. *J. Volcanol. Geotherm. Res.* **176**, 291–301 (2008).
53. Legrand, D. et al. Stress tensor analysis of the 1998–1999 tectonic swarm of northern Quito related to the volcanic swarm of Guagua Pichincha volcano, Ecuador. *Tectonophysics* **344**, 15–36 (2002).
54. van Wyk de Vries, B. et al. A gravitational spreading origin for the Socompa debris avalanche. *J. Volcanol. Geotherm. Res.* **105**, 225–247 (2001).
55. Clavero, J. E. et al. Evolution and volcanic hazards of Taapaca Volcanic Complex, Central Andes of Northern Chile. *J. Geol. Soc. (London)* **161**, 603–618 (2004).
56. Dzurisin, D. *Volcano Deformation: New Geodetic Monitoring Techniques* (Springer Science & Business Media, 2006).
57. Pezzo, G. et al. Flank sliding: a valve and a sentinel for paroxysmal eruptions and magma ascent at Mount Etna, Italy. *Geology* **48**, 1077–1082 (2002).
58. Branca, S. & Del Carlo, P. Eruptions of Mt. Etna during the past 3200 years: a revised compilation integrating the historical and stratigraphic records. In *Mt. Etna: Volcano Laboratory. Geophysical Monograph 143* (eds Bonaccorso, A., Calvari, S., Coltelli, M., Del Negro, C. & Falsaperla, S.) 1–27 (American Geophysical Union, Washington, DC, 2004).
59. Owen, S. et al. January 30, 1997 eruptive event on Kilauea Volcano, Hawaii, as monitored by continuous GPS. *Geophys. Res. Lett.* **27**, 2757–2760 (2000).
60. Wadge, G., Dorta, D. O. & Cole, P. D. The magma budget of Volcán Arenal, Costa Rica from 1980 to 2004. *J. Volcanol. Geotherm. Res.* **157**, 60–74 (2006).
61. Mastin, L. G. et al. Improved constraints on the estimated size and volatile content of the Mount St. Helens magma system from the 2004–2008 history of dome growth and deformation. *Geophys. Res. Lett.* **36**, L20304 (2009).
62. Lundgren, P. et al. Evolution of dike opening during the March 2011 Kamoamo fissure eruption, Kilauea Volcano, Hawaii. *J. Geophys. Res. Solid Earth* **118**, 897–914 (2013).
63. Kazahaya, R., Aoki, Y. & Shinohara, H. Budget of shallow magma plumbing system at Asama Volcano, Japan, revealed by ground deformation and volcanic gas studies. *J. Geophys. Res. Solid Earth* **120**, 2961–2973 (2015).
64. Anderson, K. & Segall, P. Bayesian inversion of data from effusive volcanic eruptions using physics-based models: application to Mount St. Helens 2004–2008. *J. Geophys. Res. Solid Earth* **118**, 2017–2037 (2013).
65. Kozono, T. et al. Magma discharge variations during the 2011 eruptions of Shinmoe-dake volcano, Japan, revealed by geodetic and satellite observations. *Bull. Volcanol.* **75**, 1–13 (2013).
66. Kilbride, B. M., Edmonds, M. & Biggs, J. Observing eruptions of gas-rich compressible magmas from space. *Nat. Commun.* **7**, 13744 (2016).
67. Wadge, G. & Guest, J. E. Steady-state magma discharge at Etna 1971–81. *Nature* **294**, 548–550 (1981).
68. Harris, A. et al. Thirty years of satellite-derived lava discharge rates at Etna: Implications for steady volumetric output. *J. Geophys. Res. Solid Earth* **116**, B08204 (2011).

69. Bonaccorso, A. & Calvari, S. Major effusive eruptions and recent lava fountains: balance between expected and erupted magma volumes at Etna volcano. *Geophys. Res. Lett.* **40**, 6069–6073 (2013).
70. Ganci, G. et al. Mapping volcanic deposits of the 2011–2015 Etna eruptive events using satellite remote sensing. *Front. Earth Sci.* **6**, 83 (2018).
71. Ganci, G. et al. A multi-Sensor Satellite Approach to Characterize the Volcanic Deposits Emitted during Etna's Lava Fountaining: The 2020–2022 Study Case. *Remote Sens.* **15**, 916 (2023).
72. Wasser, V. K. et al. Multidisciplinary constraints on magma compressibility, the pre-eruptive exsolved volatile fraction, and the H₂O/CO₂ molar ratio for the 2006 Augustine eruption, Alaska. *Geochem. Geophys. Geosyst.* **22**, e2021GC009911 (2021).
73. Carroll, M. R. & Holloway, J. R. Volatiles in magmas. *Mineral. Soc. Am. Rev. Mineral.* **30**, 1–517 (1994).
74. Aiuppa, A. et al. CO₂ flux emissions from the Earth's most actively degassing volcanoes, 2005–2015. *Sci. Rep.* **9**, 5442 (2019).
75. Bragagni, A. et al. A carbon-rich lithospheric mantle as a source for the large CO₂ emissions of Etna volcano (Italy). *Geology* **50**, 486–490 (2022).
76. Aiuppa et al. A SO₂ flux study of the Etna volcano 2020–2021 paroxysmal sequences. *Front. Earth Sci.* **11**, 1115111 (2023).
77. Coppola, D. et al. Monitoring endogenous growth of open-vent volcanoes by balancing thermal and SO₂ emissions data derived from space. *Sci. Rep.* **9**, 9394 (2019).
78. Calvari, S. et al. The VEI 2 Christmas 2018 Etna eruption: a small but intense eruptive event or the starting phase of a larger one? *Remote Sens.* **12**, 905 (2020).
79. Murray, J. B. The cryptic summit graben of Mt. Etna volcano. *J. Volcanol. Geotherm. Res.* **387**, 106657 (2019).
80. Duncan, A. M. et al. The 1928 eruption of Mount Etna Volcano, Sicily, and the destruction of the town of Mascali. *Disasters* **20**, 1–20 (1996).
81. Mulas, M. et al. The explosive activity of the 1669 Monti Rossi eruption at Mt. Etna (Italy). *J. Volcanol. Geotherm. Res.* **328**, 115–133 (2016).
82. Palano, M., Gresta, S. & Puglisi, G. Time-dependent deformation of the eastern flank of Mt. Etna: after-slip or viscoelastic relaxation? *Tectonophysics* **473**, 300–311 (2009).
83. Pareschi, M. T., Boschi, E. & Favalli, M. Lost tsunamis. *Geophys. Res. Lett.* **33**, L22608 (2006).
84. Palano, M. et al. GNSS-based long-term deformation at Mount Etna volcano (Italy). *Res. Geophys. Sci.* **14**, 100056 (2023).
85. Yang, X. M., Davis, P. M. & Dieterich, J. H. Deformation from inflation of a dipping finite prolate spheroid in an elastic half-space as a model for volcanic stressing. *J. Geophys. Res. Solid Earth* **93**, 4249–4257 (1988).
86. Williams, C. A. & Wadge, G. An accurate and efficient method for including the effects of topography in three-dimensional elastic models of ground deformation with applications to radar interferometry. *J. Geophys. Res. Solid Earth* **105**, 8103–8120 (2000).
87. Holland, J. H. *Adaptation in Natural and Artificial Systems*. (The University of Michigan Press, Ann Arbor, MI, 1975).
88. Amoroso, A. & Crescentini, L. Shape and volume change of pressurized ellipsoidal cavities from deformation and seismic data. *J. Geophys. Res. Solid Earth* **114**, B02210 (2009).
89. Efron, B. & Stein, C. The jackknife estimate of variance. *Ann. Stat.* **9**, 586–596 (1981).
90. Wessel, P. et al. The generic mapping tools version 6. *Geochem. Geophys. Geosyst.* **20**, 5556–5564 (2019).
91. Ganci, G., Cappello, A. & Neri, M. Data fusion for satellite-derived Earth surface: the 2021 topographic map of Etna volcano. *Remote Sens.* **15**, 198 (2022).

Acknowledgements

We thank Federico Galetto and an anonymous reviewer for their constructive comments that helped improve the manuscript. The Editor (Claire A. Currie) is acknowledged for the efficient editorial management. We thank also Mario Mattia, Daniele Pellegrino, Mario Pulvirenti, and Massimo Rossi who ensured the maintenance of the GNSS network and the acquisition of raw data. The figures were made using the GMT⁹⁰ v6.0.0 software. The GNSS data used in this study have been processed in the framework of the Project “Paroxysmal volcanic events and seaward motion at Mt. Etna: an improved picture from a geodetic and seismological perspective” (Progetti di Ricerca Libera) funded by INGV.

Author contributions

Conceptualization: M.P.; Methodology: M.P.; Resources: M.P., G.P., and C.C.; Writing-original draft: M.P., G.P., and C.C.; Writing-review and editing: M.P., G.P., and C.C.; Visualization: M.P., G.P., and C.C.; Supervision: M.P.; Funding acquisition M.P., G.P., and C.C. All authors have read and approved the final version of the manuscript.

Competing interests

The authors declare no competing interests.

Additional information

Supplementary information The online version contains supplementary material available at <https://doi.org/10.1038/s43247-024-01267-0>.

Correspondence and requests for materials should be addressed to Mimmo Palano.

Peer review information *Communications Earth & Environment* thanks Federico Galetto and the other, anonymous, reviewer(s) for their contribution to the peer review of this work. Primary Handling Editors: Teng Wang and Joe Aslin. A peer review file is available.

Reprints and permissions information is available at <http://www.nature.com/reprints>

Publisher's note Springer Nature remains neutral with regard to jurisdictional claims in published maps and institutional affiliations.

Open Access This article is licensed under a Creative Commons Attribution 4.0 International License, which permits use, sharing, adaptation, distribution and reproduction in any medium or format, as long as you give appropriate credit to the original author(s) and the source, provide a link to the Creative Commons licence, and indicate if changes were made. The images or other third party material in this article are included in the article's Creative Commons licence, unless indicated otherwise in a credit line to the material. If material is not included in the article's Creative Commons licence and your intended use is not permitted by statutory regulation or exceeds the permitted use, you will need to obtain permission directly from the copyright holder. To view a copy of this licence, visit <http://creativecommons.org/licenses/by/4.0/>.

© The Author(s) 2024